The Tensile Properties and Fracture Toughness of a Cast Mg-9Gd-4Y-0.5Zr Alloy

Zhikang Ji [1], Xiaoguang Qiao [1,*], Shoufu Guan [1], Junbin Hou [1], Changyu Hu [1], Fuguan Cong [2], Guojun Wang [2] and Mingyi Zheng [1,*]

1. School of Materials Science and Engineering, Harbin Institute of Technology, Harbin 150001, China; jzktom@163.com (Z.J.)
2. Northeast Light Alloy Company Limited, Harbin 150060, China
* Correspondence: xgqiao@hit.edu.cn (X.Q.); zhenghe@hit.edu.cn (M.Z.)

Abstract: Low fracture toughness has been a major barrier for the structural applications of cast Mg-Gd-Y-Zr alloys. In this work, the tensile properties and fracture toughness of a direct-chill-cast Mg-9Gd-4Y-0.5Zr (VW94K) alloy were investigated in different conditions, including its as-cast and as-homogenized states. The results show that the tensile properties of the as-cast VW94K alloy are greatly improved after the homogenization treatment due to the strengthening of the solid solution. The plane strain fracture toughness values K_{Ic} of the as-cast and as-homogenized VW94K alloys are 10.6 ± 0.5 and 13.8 ± 0.6 MPa·m$^{1/2}$, respectively, i.e., an improvement of 30.2% in K_{Ic} is achieved via the dissolution of the $Mg_{24}(Gd, Y)_5$ eutectic phases. The initiation and propagation of microcracks in an interrupted fracture test are observed via an optical microscope (OM) and scanning electron microscope (SEM). The fracture surfaces of the failed samples after the fracture toughness tests are examined via an SEM. The electron backscatter diffraction (EBSD) technique is adopted to determine the failure mechanism. The results show that the microcracks are initiated and propagated across the $Mg_{24}(Gd, Y)_5$ eutectic compounds in the as-cast VW94K alloy. The propagation of the main cracks exhibits an intergranular fracture pattern and the whole crack propagation path displays a zigzag style. The microcracks in the as-homogenized alloy are initiated and propagated along the basal plane of the grains. The main crack in the as-homogenized alloy shows a more tortuous fracture characteristic and a trans-granular crack propagation behavior, leading to the improvement of the fracture toughness.

Keywords: Mg-Gd-Y-Zr alloy; homogenization treatment; tensile properties; fracture toughness; crack initiation and propagation

1. Introduction

To reduce energy consumption and carbon emissions, low-density magnesium alloys have attracted great attention for their use in lightweight structures in the aerospace, automobile and electronic industries [1–3]. Unfortunately, the low levels of strength, ductility and fracture toughness of Mg alloys limit their commercial applications [4–6]. Recently, Mg-Gd-Y-Zr alloys exhibiting higher levels of strength and ductility than conventional Mg alloys have been developed [7,8]. Rare earth (RE) elements have unique physical and chemical properties due to their special extranuclear electronic structures and have become the most effective and promising alloying elements in magnesium alloys [9,10]. Among all the RE elements, Gd and Y have larger solid solubilities in Mg matrix at high temperatures, and the solid solubilities of Gd and Y decrease rapidly with a decrease in temperature [11,12]. Therefore, the addition of Gd and Y can provide significant solid-solution-strengthening and precipitation-strengthening effects. In addition, adding Gd and Y elements at the same time can reduce the solid solubility of both in the Mg matrix; thus, more second phases can be precipitated [13,14].

Some investigations have been reported concerning the microstructures and mechanical properties of Mg-Gd-Y-Zr alloys. Wang et al. [15] investigated the effect of Y for enhancing the age hardening response and mechanical properties of Mg-10Gd-xY-0.4Zr (x = 1, 3, 5 wt.%) alloys. The results showed that both the age hardening response and the tensile properties of the alloys were enhanced with an increasing Y content. Liu et al. [16] investigated the high-temperature mechanical behavior of a low-pressure sand-cast Mg-10Gd-3Y-0.5Zr alloy, which indicated that both the ultimate tensile strength and yield strength of the tested alloy firstly increased and then decreased as the temperature increased. Its elongation increased monotonously with temperature. Jiang et al. [17] investigated the effects of different Gd contents on the mechanical properties of sand-cast Mg-xGd-3Y-0.5Zr alloys. With increase in the Gd content from 9 to 11 wt.%, the amount of eutectic phase was increased, while the tensile properties were slightly decreased. The research studies on the tensile properties of as-cast Mg-Gd-Y-Zr alloys with different compositions indicated that the Mg-9Gd-4Y-0.5Zr alloy exhibited greater strength and ductility compared with the other Mg-Gd-Y-Zr alloys [17–19].

High-performance Mg-Gd-Y-Zr alloys have great potential for use in the complicated structural components of the aerospace and aircraft industries [20,21]. In order to satisfy both the reliability and safety requirements of these structural components, Mg alloys should have high fracture toughness, as well as high strength and ductility. Somekawa et al. found that the grain refinement, texture and precipitate shapes exhibited significant effects on the plane strain fracture toughness K_{Ic} of wrought magnesium alloys [22–24]. The fracture toughness of extruded pure magnesium was increased from 12.7 MPa·m$^{1/2}$ to 17.8 MPa·m$^{1/2}$ by refining the grain size from 55 μm to 1 μm due to the effect of the plastic zone [22]. An extruded AZ31 alloy with a pre-crack normal to its basal plane distribution was found to have a higher fracture toughness compared to an alloy with a pre-crack parallel to its basal plane distribution due to the difference in surface energy on the basal and non-basal planes [23]. Spherically shaped precipitates were more effective than rod-shaped precipitates for improving fracture toughness since they were more effective at pinning dislocations [24]. Lu et al. [25] reported a Mg-5Gd-2Y-0.4Zr alloy prepared via multidirectional impact forging with a tensile yield strength of 337 MPa and a static toughness of 50.4 MJ/m^3. The enhanced mechanical properties were attributed to the grain refinement in the Mg-5Gd-2Y-0.4Zr alloy. However, only a few studies on the fracture toughness K_{Ic} of cast Mg alloys have been reported in the literature. Liu et al. [26] investigated the fracture toughness and crack initiation mechanisms of a sand-cast Mg-10Gd-3Y-0.5Zr alloy. The plane strain fracture toughness of the sand-cast Mg-10Gd-0.5Zr alloy increased from 12.1 MPa·m$^{1/2}$ to 16.3 MPa·m$^{1/2}$ after T6 heat treatment (a solution treatment followed by artificial aging). For the sand-cast sample, the microcracks mainly were initiated in eutectic compounds, and the microcracks grew to become a main crack. Comparatively, the microcracks in the san-cast-T6 sample were probably initiated at the twins/α-Mg matrix and grain boundaries and propagated along the twin boundaries. The fracture morphologies indicated that the fracture mechanisms changed from the trans-granular fracture pattern of the sand-cast alloy to a mixture of intergranular and trans-granular modes in the sand-cast-T6 alloy. Wang et al. [27] found that the fracture toughness of a sand-cast Mg-6Gd-3Y-0.5Zr alloy was increased by 9.3% after it underwent a solution treatment. Compared with the as-cast sample, the as-homogenized alloy exhibited a mixture of trans-granular and intergranular fracture patterns. The as-cast alloy displayed many cleavage steps but more secondary cracks than in the as-homogenized alloy. However, the mechanisms of the initiation and propagation of microcracks in cast Mg-Gd-Y alloys remain unclear.

In this work, the microstructure, tensile properties and fracture toughness of as-cast and as-homogenized Mg-9Gd-4Y-0.5Zr alloys were investigated. And the crack initiation and propagation behaviors in interrupted fracture toughness tests were discussed in order to clarify the effect of the eutectic phase on the fracture mechanism of the alloy. The innovation of this work is that it presents the first systematic study of the fracture toughness,

crack initiation and propagation mechanisms of as-cast and as-homogenized Mg-9Gd-4Y-0.5Zr alloys, and the influence of the eutectic phase on the fracture behavior was also analyzed.

2. Materials and Experimental Procedures

2.1. Material Preparation

The magnesium alloy used in the present work was a Mg-9Gd-4Y-0.5Zr (wt.%) alloy, designated as VW94K alloy henceforth, which prepared via direct chill casting [28,29] from pure Mg (99.9 wt.%), Mg-30Gd (wt.%), Mg-30Y (wt.%) and Mg-25Zr (wt.%) in an electric resistance furnace under a mixed atmosphere of CO_2 and SF_6 at a ratio of 100:1 [30,31]. An inductively coupled plasma (ICP) analyzer was employed to analyze the chemical composition, and the actual composition of the as-cast alloy was Mg-9.12Gd-3.93Y-0.52Zr (wt.%). The homogenization treatment was performed at 510 °C for 12 h, followed by immediate warm water quenching at a temperature of ~80 °C [32,33].

2.2. Mechanical Properties

Tensile tests were conducted at a crosshead speed of 1 mm/min on a universal testing machine (Instron 5569, Norwood, MA, USA) at room temperature. The gauge length of the tensile specimens was 15 mm, with cross-sectional area of 3×2 mm^2. A 0.2% offset strength was used as the yield strength σ_{ys}. To guarantee repeatability, three tensile samples were conducted under the same conditions.

The plane strain fracture toughness tests were conducted, and the load–displacement curves were obtained using an MTS 810 servo-hydraulic fatigue tester (Eden Prairie, MN, USA). Compact tension C(T) samples (see Figure 1) with a width W = 30 mm, thickness B = 15 mm and notch depth a_0 = 12 mm were prepared according to the ASTM E399 standard [34]. Before the fracture toughness tests, a sharp fatigue pre-crack was produced under cyclic tension–tension loading and stopped until a total crack length of a = 15 mm was obtained. All samples were machined with side grooves on both surfaces, and the grooving depth was 0.1 times the sample thickness. The fracture tests were implemented at a speed of 2.5 MPa·m$^{1/2}$·s^{-1}. The stress intensity factor K_Q was calculated as in the following equation [34]:

$$K_Q = \frac{P_Q}{\sqrt{B \times B_N} \times \sqrt{W}} \cdot f\left(\frac{a}{W}\right) \tag{1}$$

where P_Q is the conditional load [34], B_N is the thickness measured at the side grooves, and $f\left(\frac{a}{W}\right)$ is the geometrical factor [34]. According to the ASTM E399 standard, K_Q can be considered the size-independent fracture toughness K_{Ic} if the test meets the following two requirements:

$$\frac{P_{max}}{P_Q} \leq 1.10 \tag{2}$$

$$2.5\left(\frac{K_Q}{\sigma_{ys}}\right)^2 \leq (W - a) \tag{3}$$

where P_{max} is the maximum load on the load–displacement curves. Three fracture toughness samples were tested for each state.
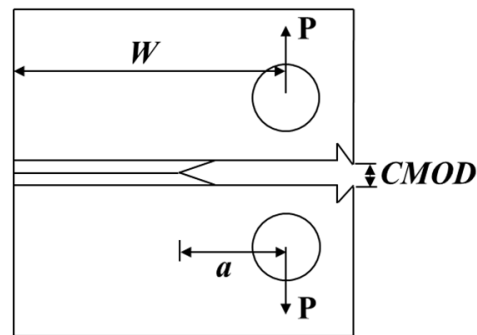
**Figure 1.** Schematic of the compact tension sample with *CMOD*.

2.3. Microstructure Characterization

The microstructural characteristics and crack propagation paths of the alloys were observed via an optical microscope (OM, Olympus PMG3, Olympus Corporation, Shinjuku, Japan) and a scanning electron microscope (SEM, ZEISS Supra 55, Carl Zeiss AG, Oberkochen, Germany) equipped with an electron backscatter diffraction instrument (EBSD, Oxford Instrument HKL, Oxford Instrument, Oxfordshire, UK). The OM and SEM samples were mechanically polished and then etched in a 4 vol% nitric acid alcohol solution. The EBSD samples were electropolished in a solution of ethanol and phosphoric acid, and the step size was 2 μm. The ESBD data were analyzed using Channel 5 software. The fracture surfaces were examined via the SEM and their three-dimensional (3D) topography was examined using a confocal laser scanning microscope (CLSM, Olympus LEXT OLS 3000, Olympus Corporation, Shinjuku, Japan). A slip trace analysis was performed via MATLAB, using an MTEX code [35].

3. Results

3.1. Microstructures

Figure 2 shows the OM and SEM microstructures of the as-cast VW94K alloy. It can be seen that the as-cast VW94K alloy is composed of an α–Mg matrix and network-shaped eutectic compounds at the grain boundaries. The average grain size, as determined via the linear intercept method [36], is about 75 μm. Based on the previous experimental results [7], the eutectic compounds in the as-cast VW94K are identified as $Mg_{24}(Gd, Y)_5$ phases.
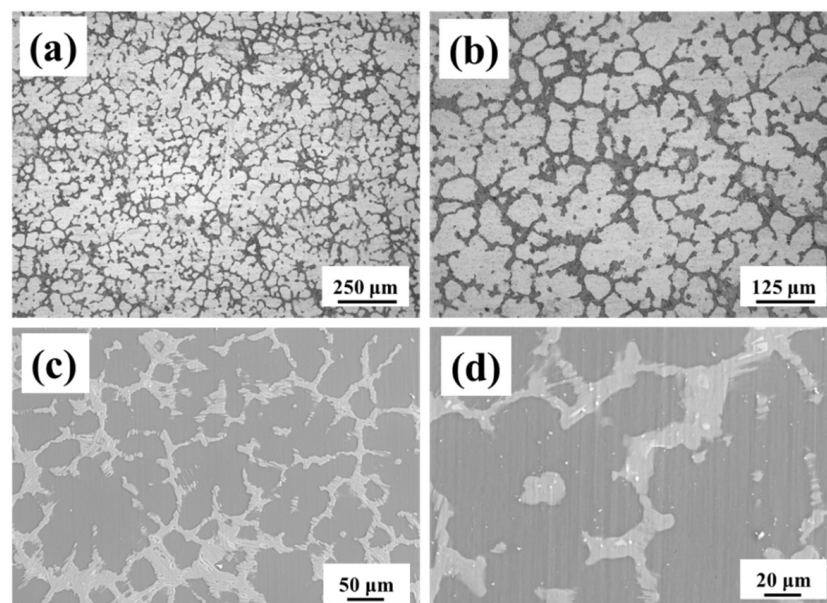
Figure 2. Microstructures of the as-cast VW94K alloy: (**a**,**b**) OM images and (**c**,**d**) SEM images.

Figure 3 shows the microstructures of the as-homogenized VW94K alloy. After the homogenization treatment at 510 °C for 12 h, the majority of the eutectic compounds of the $Mg_{24}(Gd, Y)_5$ phases were dissolved into the matrix. As shown in Figure 3d, some unevenly distributed small granular phases with white contrast are observed at the grain boundaries and within grains. These phases are determined to be RE-rich phases [32]. And the average grain size was slightly increased to 81 μm after the solution treatment.
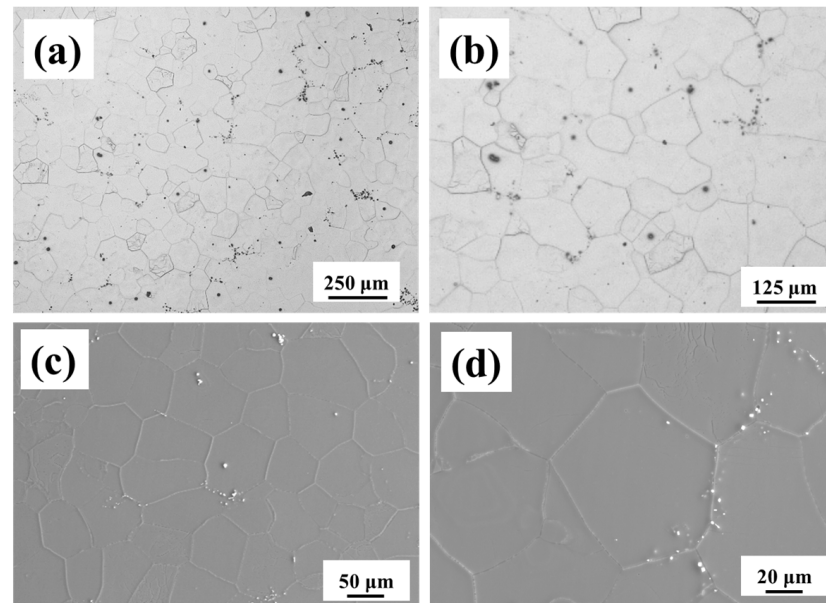
Figure 3. Microstructures of the as-homogenized VW94K alloy: (**a**,**b**) OM images and (**c**,**d**) SEM images.

3.2. Tensile Properties

Figure 4 shows the tensile engineering stress–strain curves of the as-cast and as homogenized VW94K alloys, and the values of yield strength (*YS*), ultimate tensile strength (*UTS*) and elongation to failure are summarized in Table 1. It can be seen that the as-cast VW94K alloy exhibits a *YS* of 141 MPa, a *UTS* of 205 MPa and an elongation-to-failure value of 2.5%, while the as-homogenized VW94K alloy has a YS of 165 MPa, a UTS of 233 MPa and an elongation-to-failure value of 4.6%. It can be noted that compared with the as-cast VW94K alloy, the *YS, UTS* and elongation-to-failure values of the as-homogenized alloy are improved remarkably. After the homogenization treatment, the $Mg_{24}(Gd, Y)_5$ eutectic compounds at the grain boundaries were dissolved into the matrix and formed a supersaturated solid solution, which led to a highly strengthening effect on the solid solution, reduced the microcrack initiation sites and improved the mechanical properties of the as-homogenized alloy. In a comparison of the mechanical properties of the solutioned WE43 alloy [29], the as-homogenized VW94K alloy exhibits higher yield strength and ultimate tensile strength values but shows a lower elongation-to-failure value.

Table 1. Tensile properties and fracture toughness values of the as-cast and as-homogenized VW94K alloys.

Samples	YS/MPa	UTS/MPa	Elongation to Failure/%	K_{Ic} (MPa·m$^{1/2}$)
As-cast	141 ± 3	205 ± 2	2.5 ± 0.5	10.6 ± 0.5
As-homogenized	165 ± 2	233 ± 1	4.6 ± 0.3	13.8 ± 0.6
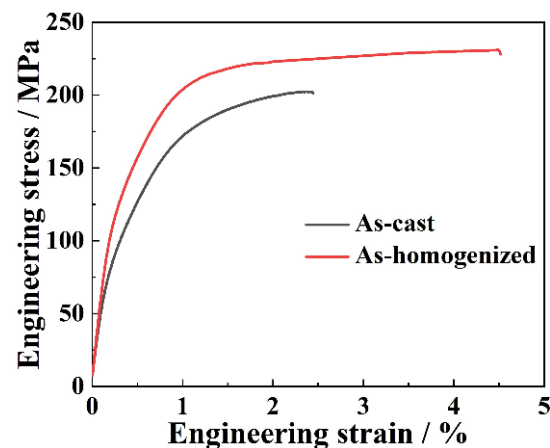
Figure 4. Tensile engineering stress–strain curves of the as-cast and as-homogenized VW94K alloys.
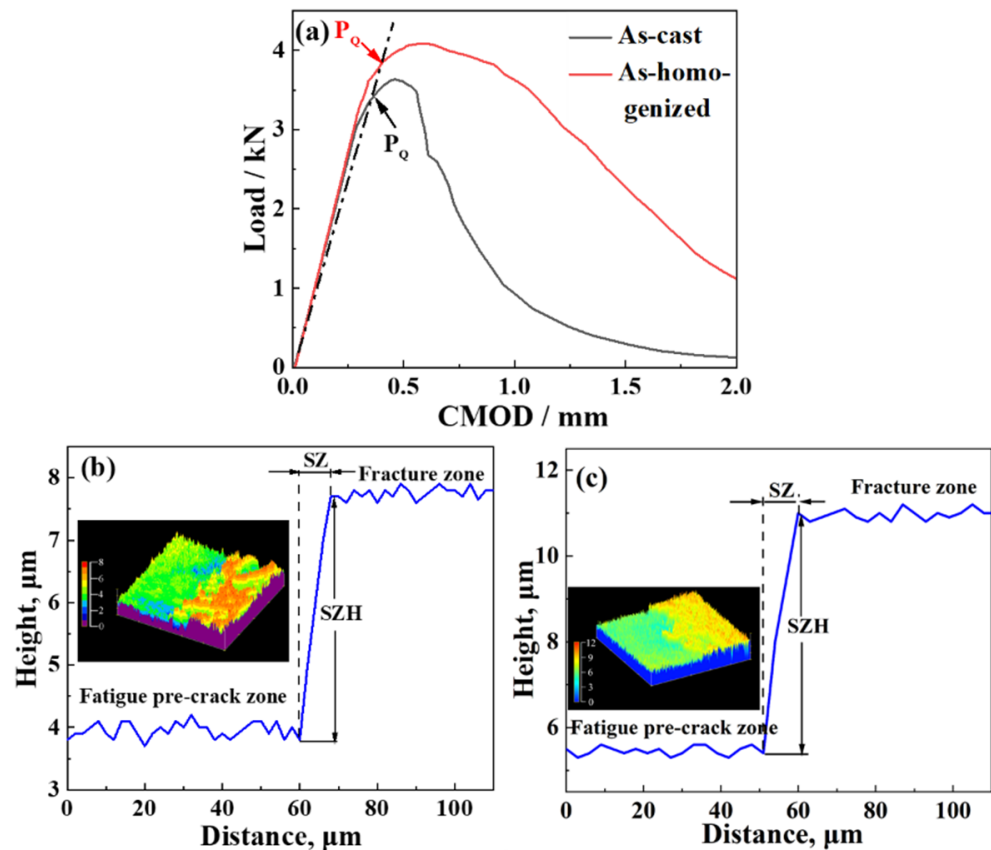
3.3. Fracture Toughness

The fracture toughness experiments were carried out with a displacement control as a function of the *CMOD*, which was obtained via the clip gauge installed on the pre-designed knife edge. The load–crack mouth opening displacement (*CMOD*) curves of the as-cast and as-homogenized VW94K alloys are presented in Figure 5a. The slopes of the linear regions in the *load–CMOD* curves are quite similar. After a linear increase in the load, both *load–CMOD* curves exhibit non-linear relationships, indicating that the crack tip underwent obvious passivation and plastic deformation. P_{max} is the resistance to the initiation of crack growth. After initiating the crack growth at P_{max}, the load gradually decreased. The corresponding conditional load P_Q and maximum load P_{max} are listed in Table 2. The maximum load for the as-homogenized VW94K alloy is greater than the maximum load for the as-cast alloy, which are 4.39 kN and 3.62 kN, respectively. In addition, the P_Q values of the as-cast and as-homogenized VW94K alloys are 2.92 kN and 3.57 kN, respectively. According to Equation (1), the stress intensity factors, K_Q, of the as-cast and as-homogenized VW94K alloys are 14.4 MPa·m$^{1/2}$ and 15.3 MPa·m$^{1/2}$, respectively. Obviously, both samples cannot meet the conditions that are expressed in Equation (2). According to the ASTM E399 [34], the stress intensity factors K_Q of the as-cast and as-homogenized VW94K alloys are invalid. Alternatively, the plane strain fracture toughness K_{Ic} can be estimated via a stretched zone (*SZ*) analysis and can be calculated according to the following equation [30,37]:

$$K_{Ic} = \sqrt{\frac{2 \times \lambda \times SZH \times E \times \sigma_{ys}}{1 - v^2}} \tag{4}$$

where λ is a constant (=2 [38]), v is Poisson's ratio (=0.35 [39]), and *SZH*, *E* and σ_{ys} are the stretched zone height, elastic modulus and yield strength, respectively. Typical cross-section profiles and three-dimensional (3D) CLSM observations of the fracture surface of the as-cast and as-homogenized VW94K alloys are shown in Figure 5b,c. It can be found that the *SZH* values of the as-cast and as-homogenized VW94K alloys are 3.9 µm and 5.6 µm, respectively. According to Equation (4), the plane strain fracture toughness (named as K_{cal}) values can be calculated to be 10.6 ± 0.5 MPa·m$^{1/2}$ and 13.8 ± 0.6 MPa·m$^{1/2}$, respectively. The values of *SZH* and fracture toughness K_{cal} are summarized in Table 2. The K_{cal} is smaller than the K_Q; hence, the K_{cal} is regarded as the plane strain fracture toughness K_{Ic}. Therefore, after the homogenization treatment, the plane strain fracture toughness K_{Ic} value increased from 10.6 ± 0.5 MPa·m$^{1/2}$ up to 13.8 ± 0.6 MPa·m$^{1/2}$.

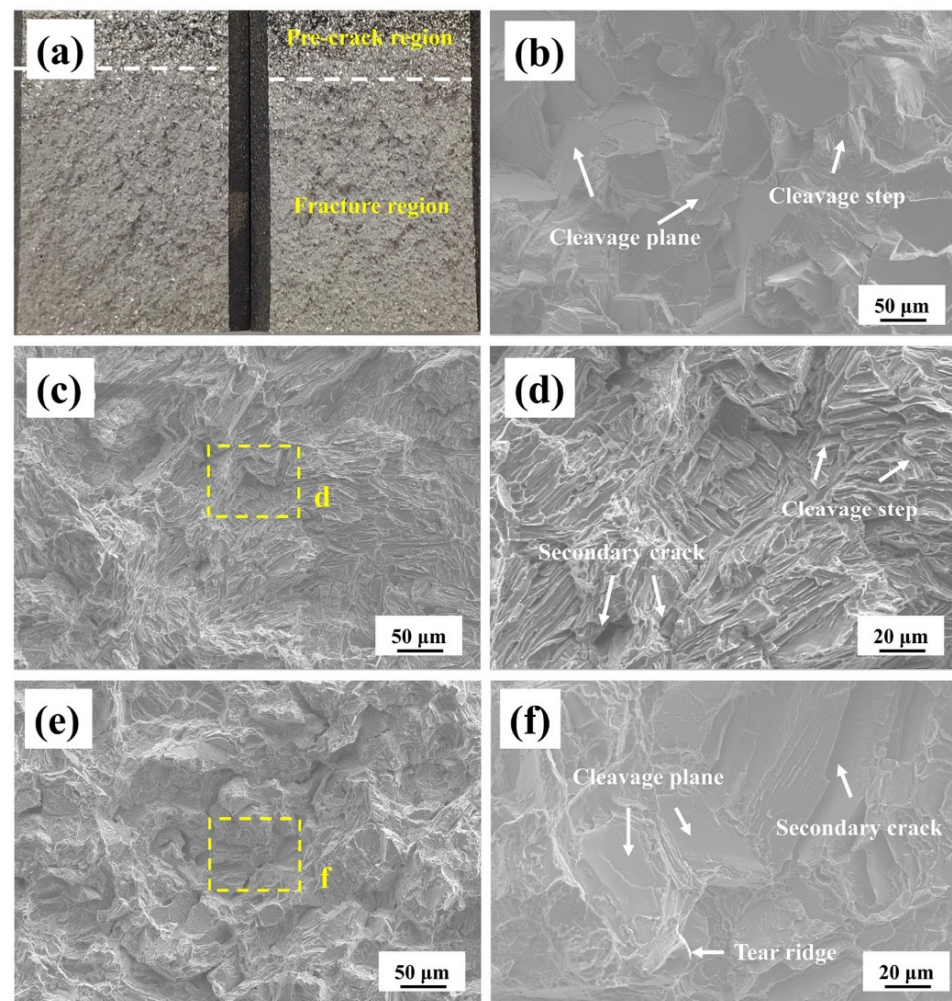**Table 2.** Results of the fracture toughness tests for the as-cast and as-homogenized VW94K alloys.

Sample	P_Q (kN)	P_{max} (kN)	K_Q (MPa·m$^{1/2}$)	P_Q/P_{max}	SZH (μm)	K_{cal} (MPa·m$^{1/2}$)	K_{Ic} (MPa·m$^{1/2}$)
As-cast	2.92	3.62	14.4 ± 0.2	1.24	3.9 ± 0.01	10.6 ± 0.5	10.6 ± 0.5
As-homogenized	3.57	4.39	15.3 ± 0.1	1.23	5.6 ± 0.01	13.8 ± 0.6	13.8 ± 0.6

Figure 5. (**a**) Load–*CMOD* curves of the as-cast and as-homogenized VW94K alloys and the cross-section profiles and 3D observations of the fracture surfaces after fracture toughness tests of (**b**) the as-cast and (**c**) the as-homogenized VW94K alloys.

4. Discussion

4.1. Fractography

The fracture surfaces of the as-cast and as-homogenized VW94K alloys after the plane strain fracture toughness tests are shown in Figure 6. It can be seen that the overall fracture surfaces of the two samples comprise pre-crack regions and fracture regions (Figure 6a). For the pre-crack region, as shown in Figure 6b, there are many cleavage planes and cleavage steps on the fracture surface. It can be seen in Figure 6c,d that the fracture region of the as-cast alloy is typical of massive cleavage steps and secondary cracks. Comparatively, there are many cleavage planes, secondary cracks and tear ridges on the fracture surface of the as-homogenized alloy (Figure 6e,f). Therefore, both the as-cast and as-homogenized samples mainly exhibit brittle fracture characteristics.

Figure 6. Fracture surfaces of the as-cast and as-homogenized VW94K alloys after fracture toughness tests: (**a**) macro-surfaces of two samples, (**b**) the fatigue pre-crack region, (**c**–**f**) the fracture regions, (**c**,**d**) the as-cast sample and (**e**,**f**) the as-homogenized sample.
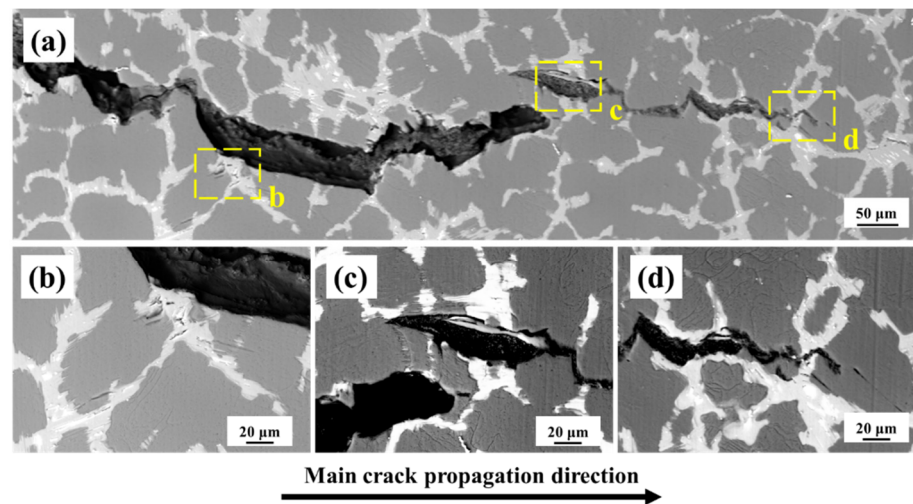
4.2. Crack Propagation Mechanism

Figure 7 shows SEM images of the crack propagation path of the as-cast VW94K alloy in an interrupted fracture toughness test. From Figure 7a, it can be seen that the whole crack propagation path displays a zigzag style. The microcracks mainly initiated in the $Mg_{24}(Gd, Y)_5$ eutectic compounds around the main crack (Figure 7b). The main crack propagates along the brittle eutectic phases at the grain boundaries near the crack tip (Figure 7c). Meanwhile, at the ahead of the crack tip, several secondary cracks initiated and propagated across the $Mg_{24}(Gd, Y)_5$ eutectic phases (Figure 7d).
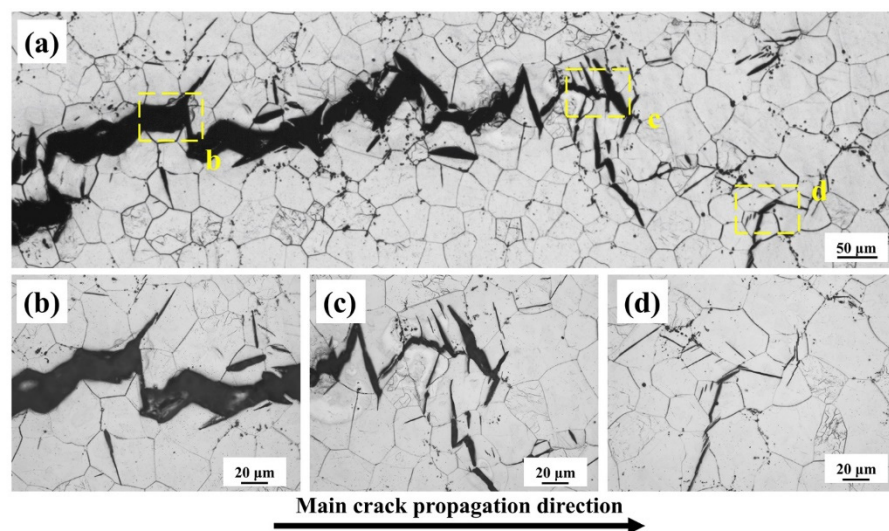
Figure 8 shows the OM images of the crack propagation path of the as-homogenized VW94K alloy in an interrupted fracture toughness test. It can be observed in Figure 8a that the as-homogenized alloy displays a more tortuous crack path than that of the as-cast alloy, which implies that more energy was consumed during crack propagation and a high level of crack propagation resistance existed. Compared with Reference [40], the fracture toughness of the as-homogenized alloy is greater than that of the LZ91 alloy, which is due to the straight path of the crack propagation in LZ91. From Figure 8b, it can be seen that the microcracks are initiated inside the grain and penetrate through the entire grain near the main crack. At the crack tip, as shown in Figure 8c, the microcracks are apt to propagate in a variety of directions. The microcracks in the same grain are parallel to each other, and these microcracks show a trend of interconnection, which can improve the fracture toughness to some extent due to the additional increase in the crack propagation paths. In

the region not far from the main crack tip (Figure 8d), it can be clearly seen that microcracks initiate inside the grain and propagate through the entire grain.


Figure 7. SEM images of the crack propagation in an interrupted fracture toughness test of as-cast VW94K alloy: (**a**) the whole crack propagation path, and in the magnification of the selected dashed rectangle: (**b**) region "b", (**c**) region "c" and (**d**) region "d" in (**a**).

Figure 8. OM images of the crack propagation of the as-homogenized VW94K alloy in an interrupted fracture toughness test: (**a**) the whole crack propagation path, and in the magnification of the selected dashed rectangle: (**b**) region "b", (**c**) region "c" and (**d**) region "d" in (**a**).

Figure 9 shows the EBSD information and microcrack morphology of the as-homogenized VW94K alloy at the crack tip of an interrupted fracture toughness test. Figure 9a,b exhibit the band contrast map and inverse pole figure (IPF) map of the sample surface. It is remarkable that most of the microcracks tend to propagate in trans-granular ways. Figure 9c–e illustrate the slip trace analysis in Grains 1, 2 and 3, as marked in Figure 9b. The theoretical slip trace directions for the following slip systems (SSs) were computed using the grain orientation information of each grain: SS 1–3 for basal slip, SS 4–6 for prismatic <a> slip and SS 7–12 for pyramidal <c + a> slip, as shown in Table 3. For Grains 1, 2 and 3, all microcracks are parallel with their basal plane. This indicates that the plastic deformation is mainly dominated by the basal slip.
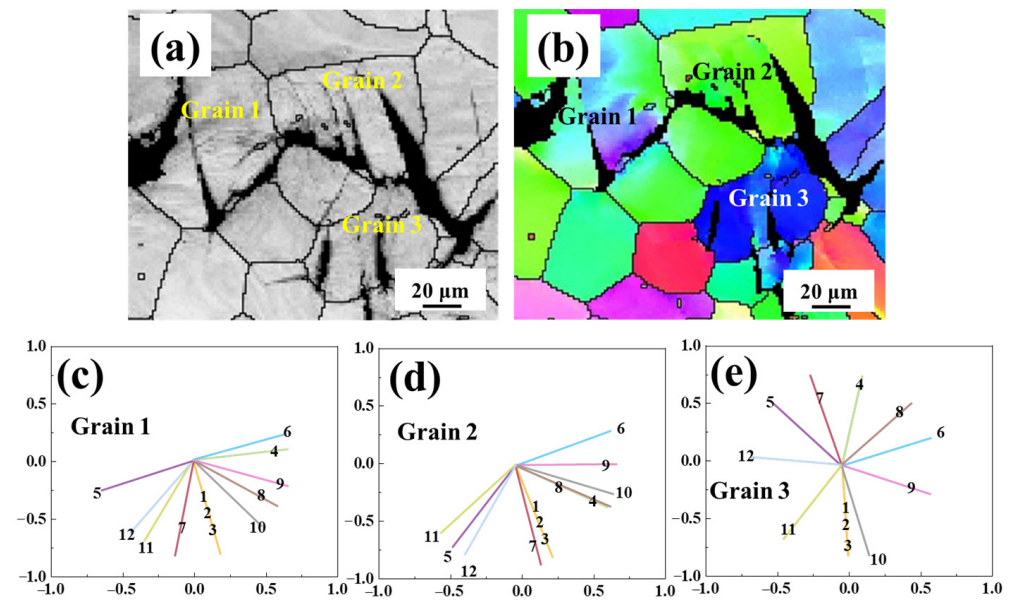
Figure 9. The typical microstructures of the as-homogenized VW94K alloy ahead of the crack tip. (**a**) Band contrast map, (**b**) inverse pole figure (IPF) map, (**c**) possible slip traces directions in Grain 1, (**d**) possible slip traces directions in Grain 2 and (**e**) possible slip traces directions in Grain 3.

Table 3. Calculated slip systems in Grains 1, 2 and 3.

Slip System Number	Slip System	
1	Basal <a>	$(0001)\ [\bar{2}110]$
2		$(0001)\ [1\bar{2}\bar{1}0]$
3		$(0001)\ [\bar{1}\bar{1}20]$
4	Prismatic <a>	$(01\bar{1}0)\ [2\bar{1}\bar{1}0]$
5		$(10\bar{1}0)\ [1\bar{2}10]$
6		$(\bar{1}100)\ [11\bar{2}0]$
7	Pyramidal <c + a>	$(11\bar{2}2)\ [\bar{1}\bar{1}23]$
8		$(\bar{1}2\bar{1}2)\ [1\bar{2}13]$
9		$(\bar{2}112)\ [2\bar{1}\bar{1}3]$
10		$(\bar{1}\bar{1}22)\ [11\bar{2}3]$
11		$(1\bar{2}12)\ [\bar{1}2\bar{1}3]$
12		$(2\bar{1}\bar{1}2)\ [\bar{2}113]$

4.3. Fracture Mechanism

After the homogenization treatment, the majority of the $Mg_{24}(Gd, Y)_5$ eutectic compounds were dissolved into the matrix, and the tensile strength, ductility and fracture toughness K_{Ic} are improved. Figure 10 shows schematic illustrations of the fracture mechanisms of the as-cast and as-homogenized VW94K alloys in interrupted fracture toughness tests. As illustrated in Figure 10a, the initiation of microcracks in the as-cast alloy was primarily caused by the $Mg_{24}(Gd, Y)_5$ phases. The microcracks then rapidly propagated along the eutectic compounds at the grain boundaries, and the intergranular microcracks were initiated. Figure 10b shows the fracture initiation and propagation of the as-homogenized alloy in an interrupted fracture toughness test. It can be seen from Figure 10b that the fracture initiation in the as-homogenized alloy during the fracture toughness test was caused by the generation of cleavage of microcracks along the basal slip bands, which is consistent with the cleavage facet features observed on the fracture surface. Then the microcracks coalesced to form longer trans-granular cracks.
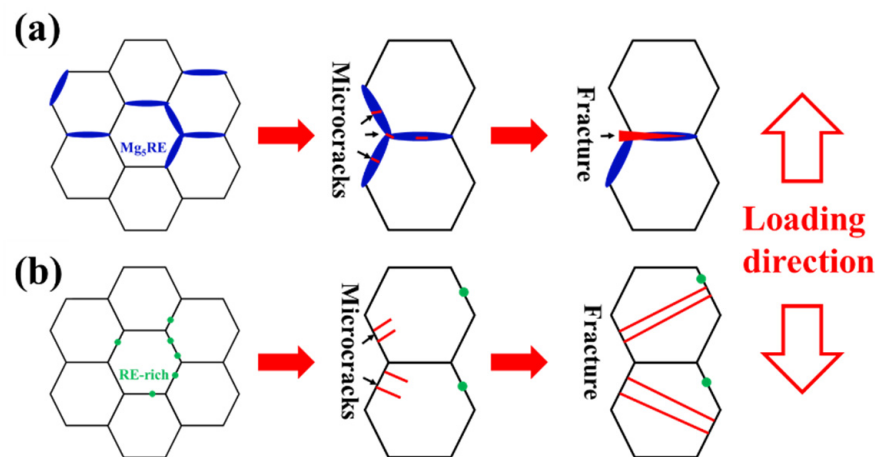
Figure 10. Schematic illustration of the fracture mechanism of the (**a**) as-cast and (**b**) as-homogenized VW94K alloys.

The coarse $Mg_{24}(Gd, Y)_5$ phases in the as-cast alloy led to dislocation accumulation and stress concentration at the grain boundaries [41]. The nucleation of microcracks first initiated at the interfaces between the eutectic phases and the α–Mg matrix, and the further coalescence of these microcracks promoted the formation of cracks [28]. After the homogenization treatment, the coarse $Mg_{24}(Gd, Y)_5$ eutectic phases were dissolved into the matrix, so the crack nucleation sites were reduced and the intrinsic resistance to crack propagation was increased, leading to the improvement of the fracture toughness.

5. Conclusions

Using OM, SEM and EBSD techniques, the present work clarified in detail the effect of $Mg_{24}(Gd, Y)_5$ eutectic compounds on the fracture toughness and fracture behaviors of the as-cast Mg-9Gd-4Y-0.5Zr (VW94K) alloy. The tensile properties and plane strain fracture toughness of the as-cast and as-homogenized VW94K alloys were investigated. The crack propagation and fracture mechanisms were discussed and the conclusions are summarized as follows:

1. Network-distributed $Mg_{24}(Gd, Y)_5$ eutectic compounds are dissolved into the matrix, and a supersaturated solid solution is obtained after homogenization treatment.
2. The as-homogenized VW94K alloy exhibits greater tensile properties than the as-cast alloy.
3. The plane strain fracture toughness K_{Ic} of the as-cast VW94K alloy is 10.6 ± 0.5 MPa·m$^{1/2}$, while that of the as-homogenized alloy is 13.8 ± 0.6 MPa·m$^{1/2}$. The improvement of 30.2% in K_{Ic} was achieved via the dissolution of the $Mg_{24}(Gd, Y)_5$ phases.
4. For the as-cast VW94K alloy, the microcracks were initiated and propagated across the $Mg_{24}(Gd, Y)_5$ eutectic compounds. The propagation of the cracks exhibits an intergranular fracture pattern, and the whole crack propagation path displays a zigzag style. Comparatively, the microcracks of the as-homogenized alloy were initiated and propagated along the basal plane. The main crack shows more tortuous fracture characteristics and a transgranular crack propagation pattern.

Author Contributions: Conceptualization, Z.J.; methodology, Z.J.; validation, Z.J. and X.Q.; investigation, Z.J., F.C. and G.W.; data curation, Z.J. and C.H.; writing—original draft, Z.J., S.G. and J.H.; writing—review & editing, X.Q. and M.Z.; supervision, X.Q. and M.Z. All authors have read and agreed to the published version of the manuscript.

Data Availability Statement: Not applicable.

Conflicts of Interest: The authors declare no conflict of interest.

References

1. Zhang, Z.; Zhang, J.; Xie, J.; Liu, S.; Fu, W.; Wu, R. Developing a Mg alloy with ultrahigh room temperature ductility via grain boundary segregation and activation of non-basal slips. *Int. J. Plast.* **2023**, *162*, 103548. [CrossRef]
2. Chen, W.; Hou, H.; Zhang, Y.; Liu, W.; Zhao, Y. Thermal and solute diffusion in α-Mg dendrite growth of Mg-5wt.%Zn alloy: A phase-field study. *J. Mater. Res. Technol.* **2023**, *24*, 8401–8413. [CrossRef]
3. Chen, L.; Zhao, Y.; Li, M.; Li, L.; Hou, L.; Hou, H. Reinforced AZ91D magnesium alloy with thixomolding process facilitated dispersion of graphene nanoplatelets and enhanced interfacial interactions. *Mater. Sci. Eng. A* **2021**, *804*, 140793. [CrossRef]
4. Song, J.; She, J.; Chen, D.; Pan, F. Latest research advances on magnesium and magnesium alloys worldwide. *J. Magnes. Alloys* **2020**, *8*, 1–41. [CrossRef]
5. Ahmad, R.; Yin, B.; Wu, Z.; Curtin, W. Designing high ductility in magnesium alloys. *Acta Mater.* **2019**, *172*, 161–184. [CrossRef]
6. Wu, S.; Qiao, X.; Zheng, M. Ultrahigh strength Mg-Y-Ni alloys obtained by regulating second phases. *J. Mater. Sci. Technol.* **2020**, *45*, 117–124. [CrossRef]
7. Pan, J.; Fu, P.; Peng, L.; Hu, B.; Zhang, H.; Luo, A. Basal slip dominant fatigue damage behavior in a cast Mg-8Gd-3Y-Zr alloy. *Int. J. Fatigue* **2019**, *118*, 104–116. [CrossRef]
8. Pan, J.; Peng, L.; Fu, P.; Zhang, H.; Miao, J.; Yue, H.; Luo, A. The effects of grain size and heat treatment on the deformation heterogeneities and fatigue behaviors of GW83K magnesium alloys. *Mater. Sci. Eng. A* **2019**, *754*, 246–257. [CrossRef]
9. Rokhlin, L. *Magnesium Alloys Containing Rare Earth Metals: Structure and Properties*; CRC Press: London, UK, 2003.
10. Zeng, Z.; Stanford, N.; Davies, C.; Nie, J.; Birbilis, N. Magnesium extrusion alloys: A review of developments and prospects. *Int. Mater. Rev.* **2019**, *64*, 27–62. [CrossRef]
11. Wu, S.; Nakata, T.; Tang, G.; Xu, C.; Wang, X.; Li, X.; Qiao, X.; Zheng, M.; Geng, L.; Kamado, S.; et al. Effect of forced-air cooling on the microstructure and age-hardening response of extruded Mg-Gd-Y-Zn-Zr alloy full with LPSO lamella. *J. Mater. Sci. Technol.* **2021**, *73*, 66–75. [CrossRef]
12. Sun, W.; Qiao, X.; Zheng, M.; He, Y.; Hu, N.; Xu, C.; Gao, N.; Starink, M. Exceptional grain refinement in a Mg alloy during high pressure torsion due to rare earth containing nanosized precipitates. *Mater. Sci. Eng. A* **2018**, *728*, 115–123. [CrossRef]
13. Sun, W.; Qiao, X.; Zheng, M.; Xu, C.; Kamado, S.; Zhao, X.; Chen, H.; Gao, N.; Starink, M. Altered ageing behaviour of a nanostructured Mg-8.2Gd-3.8Y-1.0Zn-0.4Zr alloy processed by high pressure torsion. *Acta Mater.* **2018**, *151*, 260–270. [CrossRef]
14. Sun, W.; Qiao, X.; Zheng, M.; Zhao, X.; Chen, H.; Gao, N.; Starink, M. Achieving ultra-high hardness of nanostructured Mg-8.2Gd-3.2Y-1.0Zn-0.4Zr alloy produced by a combination of high pressure torsion and ageing treatment. *Scr. Mater.* **2018**, *15*, 21–25. [CrossRef]
15. Wang, J.; Meng, J.; Zhang, D.; Tang, D. Effect of Y for, enhanced age hardening response and mechanical properties of Mg-Gd-Y-Zr alloys. *Mater. Sci. Eng. A* **2007**, *456*, 78–84. [CrossRef]
16. Liu, W.; Zhou, B.; Wu, G.; Zhang, L.; Peng, X.; Cao, L. High temperature mechanical behavior of low-pressure sand-cast Mg-Gd-Y-Zr magnesium alloy. *J. Magnes. Alloys* **2019**, *7*, 597–604. [CrossRef]
17. Jiang, L.; Liu, W.; Wu, G.; Ding, W. Effect of chemical composition on the microstructure, tensile properties and fatigue behavior of sand-cast Mg-Gd-Y-Zr alloy. *Mater. Sci. Eng. A* **2014**, *612*, 293–301. [CrossRef]
18. Wang, C.; Li, H.; He, Q.; Wu, J.; Wu, G.; Ding, W. Improvements of elevated temperature tensile strengths of Mg-Gd-Y-Zr alloy through squeeze cast. *Mater. Charact.* **2022**, *184*, 111658. [CrossRef]
19. Li, S.; Li, D.; Zeng, X.; Ding, W. Microstructure and mechanical properties of Mg-6Gd-3Y-0.5Zr alloy processed by high-vacuum die-casting. *Trans. Nonferrous Met. Soc. China* **2014**, *24*, 3769–3776. [CrossRef]
20. Li, L.; Zhang, X. Hot compression deformation behavior and processing parameters of a cast Mg-Gd-Y-Zr alloy. *Mater. Sci. Eng. A* **2011**, *528*, 1396–1401. [CrossRef]
21. Ding, Z.; Zhao, Y.; Lu, R.; Yuan, M.; Wang, Z.; Li, H.; Hou, H. Effect of Zn addition on microstructure and mechanical properties of cast Mg-Gd-Y-Zr alloys. *Trans. Nonferrous Met. Soc. China* **2019**, *29*, 722–734. [CrossRef]
22. Somekawa, H.; Mukai, T. Effect of grain refinement on fracture toughness in extruded pure magnesium. *Scr. Mater.* **2005**, *53*, 1059–1064. [CrossRef]
23. Somekawa, H.; Mukai, T. Effect of texture on fracture toughness in extruded AZ31 magnesium alloy. *Scr. Mater.* **2005**, *53*, 541–545. [CrossRef]
24. Somekawa, H.; Singh, A.; Mukai, T. Effect of precipitate shapes on fracture toughness in extruded Mg-Zn-Zr magnesium alloys. *J. Mater. Res.* **2007**, *22*, 965–973. [CrossRef]
25. Lu, S.; Wu, D.; Yan, M.; Chen, R. Achieving high-strength and toughness in a Mg-Gd-Y alloy using multidirectional impact forging. *Materials* **2022**, *15*, 1508. [CrossRef] [PubMed]
26. Liu, W.; Jiang, L.; Cao, L.; Mei, J.; Wu, G.; Zhang, S.; Xiao, L.; Wang, S.; Ding, W. Fatigue behavior and plane-strain fracture toughness of sand-cast Mg-10Gd-3Y-0.5Zr magnesium alloy. *Mater. Des.* **2014**, *59*, 466–474. [CrossRef]
27. Wang, Q.; Xiao, L.; Liu, W.; Zhang, H.; Cui, W.; Li, Z.; Wu, G. Effect of heat treatment on tensile properties, impact toughness and plane-strain fracture toughness of sand-cast Mg-6Gd-3Y-0.5Zr magnesium alloy. *Mater. Sci. Eng. A* **2017**, *705*, 402–410. [CrossRef]
28. Xu, C.; Zheng, M.; Chi, Y.; Chen, X.; Wu, K.; Wang, E.; Fan, G.; Yang, P.; Wang, G.; Lv, X.; et al. Microstructure and mechanical properties of the Mg-Gd-Y-Zn-Zr alloy fabricated by semi-continuous casting. *Mater. Sci. Eng. A* **2012**, *549*, 128–135. [CrossRef]
29. Jiang, H.; Zheng, M.; Qiao, X.; Wu, K.; Peng, Q.; Yang, S.; Yuan, Y.; Luo, J. Microstructure and mechanical properties of WE43 magnesium alloy fabricated by direct-chill casting. *Mater. Sci. Eng. A* **2017**, *684*, 158–164. [CrossRef]

30. Ji, Z.; Qiao, X.; Hu, C.; Yuan, L.; Cong, F.; Wang, G.; Xie, W.; Zheng, M. Effect of aging treatment on the microstructure, fracture toughness and fracture behavior of the extruded Mg-7Gd-2Y–1Zn-0.5Zr alloy. *Mater. Sci. Eng. A* **2022**, *849*, 143514. [CrossRef]

31. Ji, Z.; Qiao, X.; Yuan, L.; Cong, F.; Wang, G.; Zheng, M. Exceptional fracture toughness in a high-strength Mg alloy with the synergetic effects of bimodal structure, LPSO, and nanoprecipitates. *Scr. Mater.* **2023**, *236*, 115675. [CrossRef]

32. Chi, Y.; Xu, C.; Qiao, X.; Zheng, M. Effect of trace zinc on the microstructure and mechanical properties of extruded Mg-Gd-Y-Zr alloy. *J. Alloys Compd.* **2019**, *789*, 416–427. [CrossRef]

33. Chi, Y.; Liu, J.; Zhou, Z.; Wu, S.; Liu, W.; Zheng, M. Investigation on the microstructure, texture and mechanical properties of Mg-Gd-Y(-Zn)-Zr alloys under indirect extrusion. *J. Alloys Compd.* **2023**, *943*, 169061. [CrossRef]

34. *ASTM E399*; Standard Test Method for Linear-Elastic Plane-Strain Fracture Toughness of Metallic Materials. ASTM: West Conshohocken, PA, USA, 2017; pp. 1–38.

35. Zhu, G.; Wang, L.; Zhou, H.; Wang, J.; Shen, Y.; Tu, P.; Zhu, H.; Liu, W.; Jin, P.; Zeng, X. Improving ductility of a Mg alloy via non-basal <a> slip induced by Ca addition. *Int. J. Plast.* **2019**, *120*, 164–179.

36. *ASTM E112*; Standard Test Methods for Determining Average Grain Size. ASTM: West Conshohocken, PA, USA, 2012.

37. Taisuke, S.; Somekawa, H.; Takara, A.; Nishikawa, Y.; Higashi, K. Plane-strain fracture toughness on thin AZ31 wrought magnesium alloy sheets. *Mater. Trans.* **2003**, *24*, 986–990.

38. Higashi, K.; Ohnishi, T.; Komatsu, K.; Nakatani, Y. Evaluation of fracture toughness of 5083 and 7075 alloys by stretched zone analysis. *J. Jpn. Inst. Light Met.* **1981**, *31*, 720. [CrossRef]

39. Handbook, A. *Magnesium and Magnesium Alloys, Materials Park*; ASM International: West Conshohocken, PA, USA, 1999.

40. Rahmatabadi, D.; Pahlavani, M.; Bayati, A.; Hashemi, R.; Marzbanrad, J. Evaluation of fracture toughness and rupture energy absorption capacity of as-rolled LZ71 and LZ91 Mg alloy sheet. *Mater. Res. Express.* **2019**, *6*, 36517. [CrossRef]

41. Lu, X.; Zhao, G.; Zhou, J.; Zhang, C.; Yu, J. Microstructure and mechanical properties of the as-cast and as-homogenized Mg-Zn-Sn-Mn-Ca alloy fabricated by semicontinuous casting. *Materials* **2018**, *11*, 703. [CrossRef]